Journal of Materials Chemistry A

ROYAL SOCIETY OF CHEMISTRY

PAPER

View Article Online
View Journal | View Issue

Cite this: J. Mater. Chem. A, 2023, 11, 3575

Mapping polymer donors with a non-fused acceptor possessing outward branched alkyl chains for efficient organic solar cells†

Qing Shen,‡[a] Chengliang He,‡[a] Shuixing Li,*[a] Lijian Zuo,[ab] Minmin Shi [a] and Hongzheng Chen *[a]

Developing non-fused-ring electron acceptors (NFREAs) is a promising strategy toward high-efficiency and low-cost organic solar cells (OSCs), for which an in-depth understanding of the donor:acceptor (D:A) pairing principles is essential. Herein, we designed and synthesized a tetra-thiophene-cored NFREA with outward branched alkyl chains, BO-4T, and performed a systematic study by mapping four polymer donors, namely D18, PM6, PBDB-T, and J52, with BO-4T to investigate the carrier dynamics and molecular packing. It was unveiled that the narrowed energetic offset and broadened absorption coverage of the D:A blends were favorable for maximizing the voltage and photocurrent of OSCs, respectively, and the suitable phase separation induced by the miscibility between the D:A couple was critical for achieving high crystallinity and good charge-transport properties. Finally, with lower energy loss and less charge recombination, PM6 worked the best with BO-4T, demonstrating a high efficiency of 14.33%, which is among the best for OSCs based on NFREAs. Therefore, this work provides valuable guidelines for selecting polymer donors to match NFREAs.

Received 6th December 2022
Accepted 16th January 2023

DOI: 10.1039/d2ta09500a

rsc.li/materials-a

Introduction

As a kind of clean energy utilization technology, organic solar cells (OSCs) have received increasing attention in recent years due to their unique characteristics, such as flexibility, colorfulness, and translucency.[1–3] For efficient OSCs, the photoactive layer mainly adopts a bulk-heterojunction (BHJ) structure, consisting of a p-type compound as the electron donor (D) and n-type compound as the electron acceptor (A).[4,5] With both efforts in developing wide bandgap donors, *e.g.*, PM6 and D18, and narrow bandgap non-fullerene acceptors (NFAs), *e.g.*, Y6 and L8-BO, single-junction OSCs have shown their potential in achieving power conversion efficiencies (PCEs) of over 19%, thus showing promise toward commercialization applications.[6–17] However, to realize the economic benefits of commercial applications the applied photoactive materials should possess both high efficiency and low cost,[18,19] while the current champion efficiencies were achieved with complicated fused-ring Y-series NFAs, thus building barriers toward large-scale applications.[20] Based on this, relative to fused-ring electron acceptors (FREAs), non-fused-ring electron acceptors (NFREAs) with broken fused-ring structures and easier synthesis procedures have caught the attention of researchers.[18,21–23]

Early in 2018, our group proposed an approach involving utilizing noncovalent intramolecular interactions, *e.g.*, F···H interactions, for replacing the fused structure to design NFREAs, yielding DF-PCIC with an efficiency over 10% and high thermal stability.[24] Such a design also reduced the synthetic steps, thus lowering the material costs. Later, a more simplified NFREA, ICTP consisting of only one benzene ring and two thiophene rings as the molecular backbone and O···H intramolecular interaction, was also designed by our group. Further modifications of an outward linear alkyl chain on the thiophene ring and fluorination on the terminals led to a PCE of over 10% in such a completely non-fused structure.[25,26] Bo *et al.* also reported tetra-thiophene rings as a feasible choice for constructing NFREAs and an efficiency over 12% could be achieved by altering the substituted alkyl chains on the four thiophene rings.[27] Very recently, based on a tetra-thiophene ring backbone, Hou *et al.* introduced rigid 2,4,6-triisopropylphenyl as the substituent for the central bi-thiophene rings, yielding A4T-16. Such an arrangement enabled a 3D-interpenetrated crystalline structure, leading to a high PCE of 15.2% with an outstanding fill factor (FF) of 0.798.[28] Continuous efforts have investigated NFREAs for higher efficiencies, but mainly focus on how the

[a]State Key Laboratory of Silicon Materials, MOE Key Laboratory of Macromolecular Synthesis and Functionalization, International Research Center for X Polymers, Department of Polymer Science and Engineering, Zhejiang University, Hangzhou 310027, P. R. China. E-mail: lishuixing89@163.com; hzchen@zju.edu.cn

[b]Zhejiang University-Hangzhou Global Scientific and Technological Innovation Center, Hangzhou 310014, P. R. China

† Electronic supplementary information (ESI) available. CCDC 2223269. For ESI and crystallographic data in CIF or other electronic format see DOI: https://doi.org/10.1039/d2ta09500a

‡ These authors contributed equally to this work.

molecular structures of NFREAs affect the device performance.[18,29–36] Less attention has been devoted to the polymer donors mapping with a NFREA, which is critical, since the crystallization dynamics in the BHJ photoactive layer are controlled by the both donor and acceptor.[4,37] An understanding of how varied polymer donors regulate the crystalline packing of the photoactive layer with a NFREA is essential to guide the future design of highly efficient OSCs based on low-cost NFREAs.

Under the above backgrounds, we here performed a study on mapping the polymer donors with a NFREA. First, based on the tetra-thiophene ring backbone, we designed and synthesized a NFREA with high steric 2,4,6-triisopropylphenyl as the substituents on the central bi-thiophene rings and outward branched alkyl chains, 2-butyloctyl (2-BO), as the substituents on another two thiophene rings, yielding BO-4T (Fig. 1). The crystalline packing structure study of BO-4T *via* single-crystal analysis revealed condensed π–π stacking and a predominant face-on molecular orientation, beneficial for superior charge transport in the acceptor domains. Then, four wide bandgap polymer donors of D18, PM6, PBDB-T, and J52 were selected to pair with BO-4T for a systematical study on D–A matching in NFREA-based OSCs (see Fig. 1a for the chemical structures). The effects of the polymer donors' energetics, absorption, and aggregation properties on the carrier dynamics and crystallization behaviors, and thus the whole device performances were investigated. With more benefits in voltage and FF, the D–A combination of PM6:BO-4T demonstrated the highest PCE of 14.33%, representing one of the highest efficiencies for NFREA-based OSCs. When evaluating the cost and performance of the materials, BO-4T possessed a prominent figure-of-merit (FOM) value of 23.25 among several representative acceptors, indicating its advantage in terms of low material costs.

Results and discussion

Molecular design and quantum chemistry calculations

The synthetic route for the non-fused acceptor BO-4T is shown in Fig. 1b. Compound **2** was obtained *via* a Suzuki coupling of brominated dithiophene and (2,4,6-triisopropylphenyl)boronic acid. Then the two α-hydrogen atoms of **2** were replaced by bromine atoms, thus obtaining compound **3**. Compound **4** was

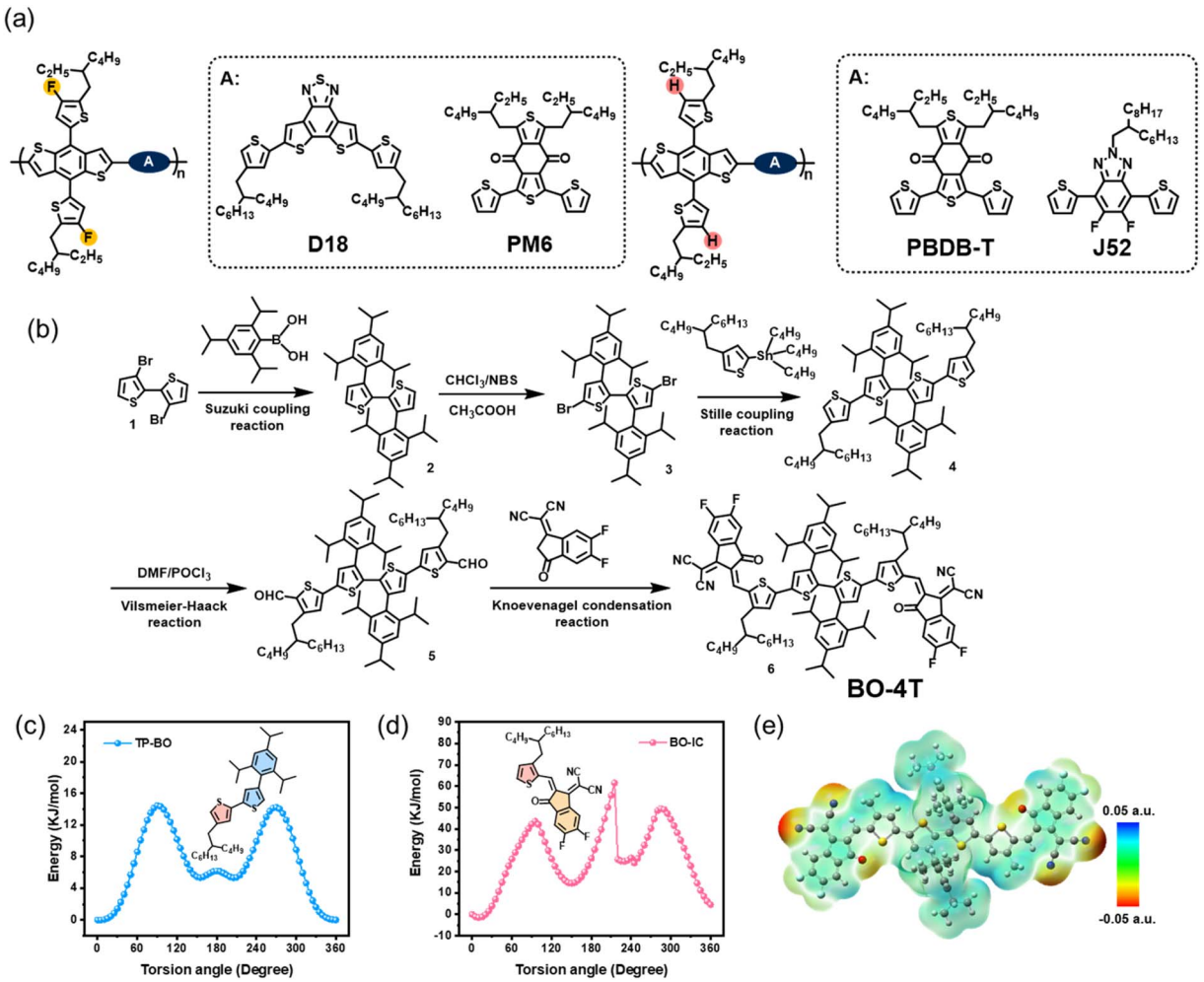

Fig. 1 (a) Chemical structures of D18, PM6, PBDB-T, and J52. (b) Synthetic route for BO-4T. (c) Internal rotation barrier of TP-BO. (d) Internal rotation barrier of BO-IC. (e) ESP distribution for BO-4T at the B3LYP/6-31 G(d,p) level.

derived from the Stille coupling of **3** and tributyl(4-(2-butyloctyl) thiophen-2-yl)stannane. Afterwards, the dialdehyde intermediate **5** was obtained by a Vilsmeier–Haack reaction. Finally, the Knoevenagel condensation of **5** and 2-(5,6-difluoro-3-oxo-2,3-dihydro-1*H*-inden-1-ylidene)malononitrile derived the target molecule BO-4T. BO-4T exhibited excellent solubility in common solvents like CH_2Cl_2 and $CHCl_3$, and the chemical structure was verified by ^{1}H NMR, ^{13}C NMR spectroscopy, and matrix-assisted laser desorption/ionization time of flight (MALDI-TOF) mass spectrometry (Fig. S1–S7†). The detailed synthesis and characterization of BO-4F can be found in the ESI.†

Density functional theory (DFT) theoretical calculations were performed at the B3LYP/6-31 G(d,p) level for obtaining the optimal geometry, and showed a planar conformation for BO-4T (Fig. S8†), favoring the packing of adjacent molecules. To verify the effects of 2,4,6-triisopropylphenyl and 2-BO substituents on the geometry, the internal rotation barrier between two adjacent structural units was calculated (Fig. 1c and d). TP-BO was the molecular fragment composed of the thiophene unit in the core and π-bridge, and BO-IC was composed of a π-bridge and terminal. It was found that the *trans* conformation of two thiophene rings was the more stable state than the *cis* conformation for TP-BO. As for BO-IC, the outward branched alkyl chains induced strong steric hindrance effects, making the conformation with the formation of O···S noncovalent interaction the stable state and inducing an especially large rotation barrier (~45.0 kJ mol^{-1}) from the stable state to the meta-stable state ($E_{s\rightarrow ms}$). Besides, 2,4,6-triisopropylphenyl and 2-BO substituents helped endow BO-4T with a planar geometry, which was beneficial for intramolecular charge transfer and intermolecular charge transport. In addition, the electrostatic potential (ESP) distribution of BO-4T was also calculated and is depicted in Fig. 1e. The positive ESP distributions suggested its good electron-accepting capacity.[38]

Molecular characterization and single-crystal structure analysis

The optical property of BO-4T was characterized by ultraviolet-visible (UV-vis) spectroscopy (Fig. 2a). BO-4T exhibited broad absorption ranging from 500 to 800 nm with a peak centered at 718 nm in $CHCl_3$ solution. While in thin film, the maximal absorption peak was red-shifted by 60 nm with an absorption edge located at 868 nm. Besides, the film absorption peak of BO-4T indicated strong *J*-aggregation, which could facilitate efficient charge transport.[39,40] The energy levels of BO-4T were measured through cyclic voltammetry (Fig. 3b and S9†). The lowest unoccupied molecular orbital (LUMO) and highest occupied molecular orbital (HOMO) levels of BO-4T were −3.90 and −5.65 eV, respectively. Further, molecular stacking and orientation of the pristine BO-4T film were analyzed through grazing incidence wide-angle X-ray scattering (GIWAXS), as shown in Fig. 2b and c.[41] A notable (001) diffraction peak at q_r = 0.238 Å^{-1} in the in-plane (IP) direction could be distinguished, corresponding to a lamellar stacking distance of 26.4 Å, and a weaker lamellar stacking (002) peak located at q_r = 0.452 Å^{-1}, corresponding to a lamellar stacking distance of 13.9 Å. The presence of the (001) and (002) diffraction peaks implied the existence of long-range backbone ordering.[42] As for the out-of-plane (OOP) direction, a strong (010) diffraction peak could be

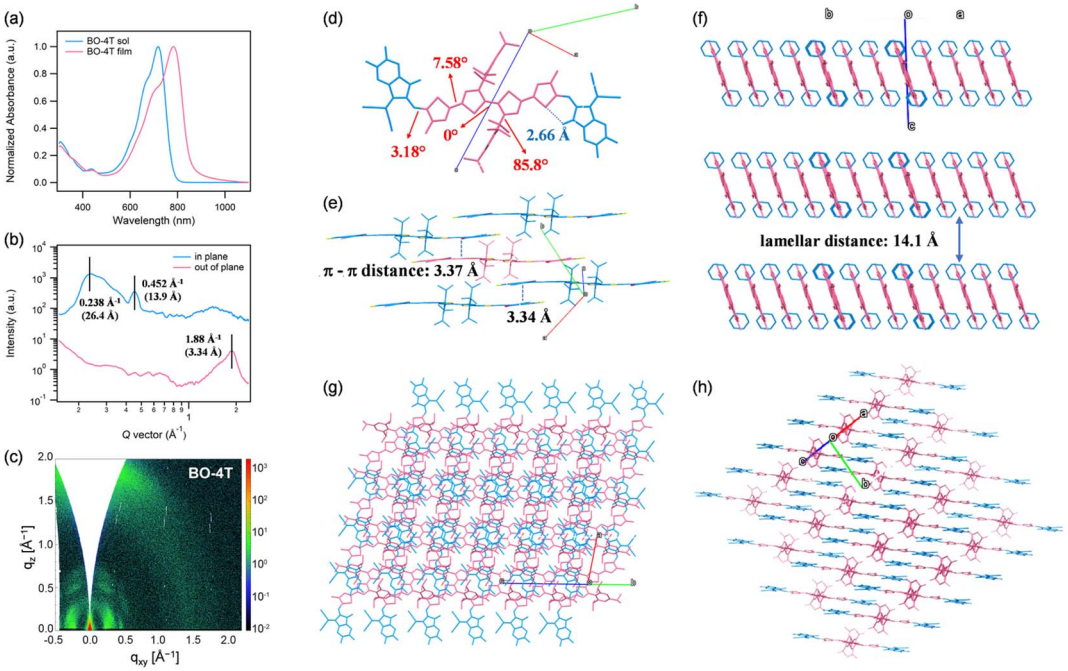

Fig. 2 (a) UV-vis absorption spectra of BO-4T in $CHCl_3$ solution and thin film. (b) GIWAXS scattering intensity profiles along the in-plane and out-of-plane directions of BO-4T film. (c) 2D GIWAXS image of the pristine BO-4T film. (d) Single-crystal structure of BO-4T (CCDC: 2223269). (e) Crystal-packing structure of BO-4T. (f–h) Multi-molecular configurations extracted from the single-crystal structure.

observed at $q_z = 1.88$ Å^{-1}, corresponding to a compact π–π stacking distance of 3.34 Å. The above results indicated that BO-4T formed condensed π–π stacking and mainly adopted a face-on molecular orientation, which is beneficial to carrier transport.[43]

The single crystal of BO-4T was obtained *via* the liquid diffusion method in order to gain an in-depth understanding of the molecular geometry and intermolecular stacking. The molecular configuration is shown in Fig. 2d. The two thiophenes in the core were in the same plane with a dihedral angle close to 0°. While the dihedral angle between the core and the attached thiophene π-bridge was 7.58°, and the dihedral angle between the π-bridge and terminal was 3.18°. The distance between the sulfur atom in the π-bridge and the oxygen atom in the end group was 2.66 Å, smaller than the sum of the S and O van der Waals radii (3.32 Å), indicating the formation of O···S interaction. Meanwhile, the rigid group in the core was almost perpendicular to the thiophene ring, which was able to inhibit over-sized intermolecular aggregation. Both the conformation in the single crystal and the geometry obtained *via* the DFT calculations mentioned above verified the good planarity of BO-4T. Furthermore, it can be seen from Fig. 2e that effective π–π stacking was formed between the end groups, and the π–π stacking distances between the end groups were 3.37 and 3.34 Å, agreeing well with the GIWAXS results. The small π–π stacking distances may be ascribed to the good molecular planarity. The value of lamellar packing distance calculated from the GIWAXS scattering profile could also be found in the single-crystal diffraction analysis (Fig. 2f), which revealed that the crystalline nature of BO-4T could be maintained in the spin-coated film to some extent.[11,44] As shown in Fig. 2g and h, the intermolecular stacking of BO-4T was highly regular with effective *J*-aggregation, which was consistent with the *J*-aggregation observed in film absorption, which is conducive to the formation of effective intermolecular charge-transfer channels.[39] The above results indicate that through rational structure design, the obtained BO-4T had a defined molecular conformation and favorable stacking behaviors with a face-on molecular orientation in the thin film, which provides a good case for rationally designing NFREAs.

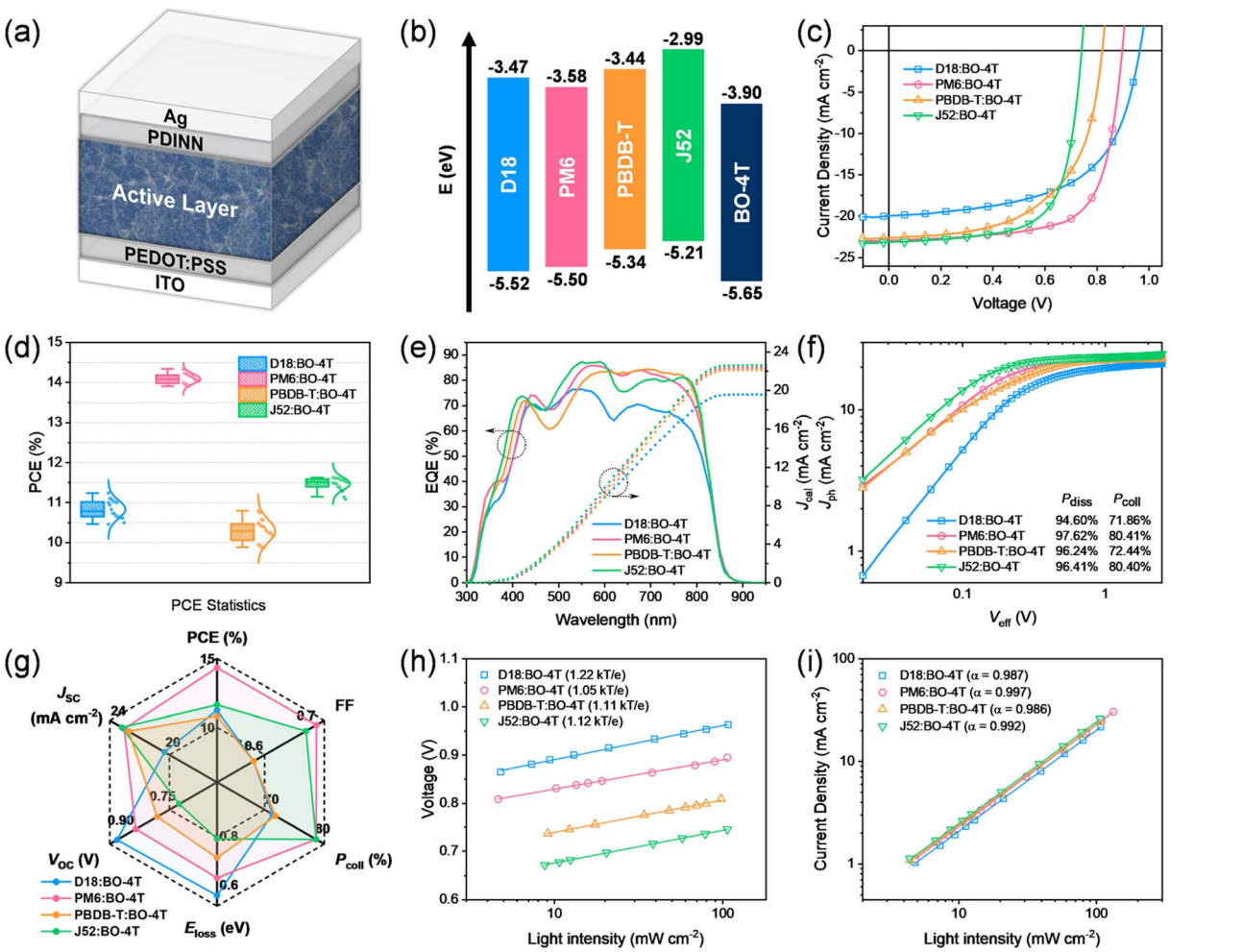

Fig. 3 (a) Schematic illustration of the conventional device structure. (b) Schematic energy level alignment of the studied materials. (c) *J*–*V* curves of the optimal devices. (d) PCE statistics of 20 cells for each blend. (e) EQE curves and integral current curves of the optimal devices. (f) J_{ph}–V_{eff} curves of the optimal devices. (g) Radar graph of the average photovoltaic parameters of the optimal devices. (h) Dependencies of the voltage on the light intensity of the optimal devices. (i) Dependencies of the current density on the light intensity of the optimal devices.

Photovoltaic properties and recombination mechanism

With BO-4T as the acceptor, we selected D18 and PM6 with a fluorinated benzodithiophene (BDT) unit as well as PBDB-T and J52 with a non-fluorinated BDT unit, as polymer donors to perform a comparable study.[6,7,45,46] These four polymer donors possessed complementary absorption to BO-4T (Fig. S10†) and gradually lifted HOMO levels from −5.52 eV for D18 to −5.21 eV for J52 (Fig. 3b). We then fabricated the devices with a conventional structure to characterize the photovoltaic properties (Fig. 3a). The device preparation conditions were well optimized and are summarized in Table S1†. The current density–voltage (*J*–*V*) curves of the optimal OSCs are shown in Fig. 3c, and the photovoltaic parameters are listed in Table 1. Fig. 3d shows the PCE data statistics. The open-circuit voltage (V_{OC}) was reduced from 0.964 V and 0.897 V for D18:BO-4T-based and PM6:BO-4T-based devices to 0.820 V and 0.741 V for PBDB-T:BO-4T-based and J52:BO-4T-based devices, in line with the gradually lifted HOMO levels for these polymer donors. As a result, the calculated energy losses for D18:BO-4T, PM6:BO-4T, PBDB-T:BO-4T, and J52:BO-4T-based devices were 0.524, 0.596, 0.678, and 0.756 eV, respectively, indicating that reducing the HOMO offset between the donor and acceptor is a feasible way to lower the energy loss.[47]

For the short-circuit current density (J_{SC}), except for the D18:BO-4T system, all the other three systems demonstrated high J_{SC} values of ~23 mA cm^{-2}, illustrating that lowering the driving force was not the main barrier to achieving efficient charge separation in the non-fullerene systems. However, the D18:BO-4T system exhibited a significantly lower J_{SC} of 19.97 mA cm^{-2} despite it having the lowest energy loss, which was related with an unfavorable blend morphology and severe charge recombination, as discussed below. The highest J_{SC} of the J52:BO-4T system benefited from a broader absorption coverage in the short-wavelength range (Fig. 3e), which was consistent with the absorption spectrum of the blend films (Fig. S11†).

As for the FF, it varied largely. The highest FF of 0.70 was achieved for the PM6:BO-4T-based device, and the second highest FF of 0.68 was achieved for J52:BO-4T-based device. For comparison, a worse FF of 0.58 was presented in both D18:BO-4T-based and PBDB-T:BO-4T-based devices. These observations implied there may exist significant differences in the blend morphology or crystalline behaviors among these four systems.[41,48]

Combining all the above, the PM6:BO-4T system performed well in terms of all three device parameters, thus resulting in the best PCE of 14.33%, while the other three systems showed worse performances, with PCEs varying between 10.80–11.63%, due to shortcomings either in the voltage or fill factor.

Next, external quantum efficiency (EQE) tests were carried out to cross-check the photocurrent generation, and the results are shown in Fig. 3e and Table 1. Except for the D18:BO-4T-based device, the other three devices exhibited an over 80% photon-to-electron response from 500 to 800 nm. The integrated J_{cal} values from the EQE curves were 19.56, 22.37, 22.12, and 22.60 mA cm^{-2} for OSCs based on D18:BO-4T, PM6:BO-4T, PBDB-T:BO-4T, and J52:BO-4T, respectively, in accordance with those derived from their *J*–*V* curves.

In order to investigate the charge-transport properties of the blend films, space-charge-limited current (SCLC) tests were conducted in hole-only devices (ITO/PEDOT:PSS/active layer/MoO_3/Ag) and electron-only devices (ITO/ZnO/active layer/PDINN/Ag) to measure the hole and electron mobilities (Fig. S12†). The PM6:BO-4T blend possessed the highest electron mobility (μ_e) of 9.40 × 10^{-4} cm^2 V^{-1} s^{-1} and the highest hole mobility (μ_h) of 8.65 × 10^{-4} cm^2 V^{-1} s^{-1}, giving the most balanced μ_e/μ_h ratio of 1.09. The J52:BO-4T blend was the next best, with a μ_e of 7.49 × 10^{-4} cm^2 V^{-1} s^{-1} and a μ_h of 4.33 × 10^{-4} cm^2 V^{-1} s^{-1}, giving a μ_e/μ_h ratio of 1.73. The high carrier mobility and balanced μ_e/μ_h ratio contributed to the excellent J_{SC}s and FFs of PM6:BO-4T- and J52:BO-4T-based OSCs. In contrast, the D18:BO-4T blend exhibited the lowest μ_e of 2.32 × 10^{-4} cm^2 V^{-1} s^{-1} and a relatively low μ_h of 1.33 × 10^{-4} cm^2 V^{-1} s^{-1}, giving a μ_e/μ_h ratio of 2.13, while the PBDB-T:BO-4T blend possessed a relatively high μ_e of 6.40 × 10^{-4} cm^2 V^{-1} s^{-1} but an extremely low μ_h of 0.25 × 10^{-4} cm^2 V^{-1} s^{-1}, resulting in the least balanced μ_e/μ_h ratio of 25.13, which led to awful J_{SC} and FF values for devices based on D18:BO-4T and PBDB-T:BO-4T.

To further explore the photon-to-electron process for understanding the differences in the device parameters, we studied the relationship between the photocurrent density and effective voltage of the OSCs (Fig. 3f) to explore the bias-dependent exciton-dissociation and charge-collection behaviors. Photocurrent density (J_{ph}) *versus* effective voltage (V_{eff}) curves were used to evaluate the exciton-dissociation efficiencies (P_{diss}s) and charge-collection efficiencies (P_{coll}s) in OSCs.[49] The results showed that the OSC based on PM6:BO-4T possessed the highest P_{diss} (97.62%) and P_{coll} (80.41%), followed by the J52:BO-4T-based device, which was consistent with the high J_{SC} and FF values in the PM6:BO-4T and J52:BO-4T systems. By contrast, the P_{diss} and P_{coll} of the D18:BO-4T-based OSC were the lowest (94.60% and 71.86%, respectively),

Table 1 Photovoltaic parameters of OPVs based on different donors

Active layer	V_{OC} (V)	J_{SC} (mA cm^{-2})	J_{cal}[a] (mA cm^{-2})	FF	PCE[b] (%)	E_{loss}[c] (eV)
D18:BO-4T	0.964 (0.958 ± 0.007)	19.97 (20.14 ± 0.36)	19.56	0.58 (0.56 ± 0.01)	11.24 (10.83 ± 0.23)	0.524
PM6:BO-4T	0.897 (0.896 ± 0.002)	22.94 (22.79 ± 0.13)	22.37	0.70 (0.69 ± 0.00)	14.33 (14.09 ± 0.12)	0.596
PBDB-T:BO-4T	0.820 (0.821 ± 0.004)	22.62 (22.46 ± 0.30)	22.12	0.58 (0.56 ± 0.01)	10.80 (10.29 ± 0.28)	0.678
J52:BO-4T	0.741 (0.745 ± 0.003)	23.11 (23.02 ± 0.35)	22.60	0.68 (0.67 ± 0.01)	11.63 (11.47 ± 0.16)	0.756

[a] Integrated current densities from EQE curves. [b] Average PCEs from 20 devices. [c] Energy loss was calculated *via* the equation of $E_{loss} = E_g - qV_{OC}$.

which indicated an inefficient charge generation for the lower J_{SC} and FF, and so it was for the PBDB-T:BO-4T system. From the radar plots of six device parameters (Fig. 3g), we could easily identify that the D18, PBDB-T, and J52-based systems have both merits and demerits, while the PM6-based system performed the most comprehensively.

Furthermore, the dependences of J_{SC} and V_{OC} on the light intensity (P_{light}) were tested to explore the charge recombination in devices. The slopes (n) obtained from the equation $V_{OC} \propto nkT/q\ln(P_{light})$ could be used as an indicator for identifying the recombination behavior, where a larger n represents a higher proportion of monomolecular recombination.[50] It was found that the D18:BO-4T blend exhibited the highest proportion of monomolecular recombination, which may be due to the formation of large phase-separation domains, while PM6:BO-4T could suppress the monomolecular recombination. The relationship between J_{SC} and P_{light} could be described as $J_{SC} \propto P_{light}^{\alpha}$, where the closer the α value is to 1, the lower a component of bimolecular recombination exists.[50] It is worth mentioning that the α of the PM6:BO-4T-based OSC was the highest (0.997), implying the least extent of bimolecular recombination. The recombination situations verified the best performance of the PM6:BO-4T system.

In order to evaluate the photoelectric performance *versus* the synthetic complexity (SC) of BO-4T-based OSCs, we calculated the figure-of-merit (FOM = PCE/SC) value of BO-4T and compared it with those of some other classic acceptors (Y6, BTP-eC9, IT-4F, ITIC, and DF-PCIC), and the detailed calculation process is listed in the ESI (Fig. S13–S18 and Table S2†). The result showed that BO-4T had the highest FOM owing to its lowest SC, which indicated the potential of BO-4T in the fabrication of OSCs with high efficiency and low cost.

Morphological characteristics

To identify the morphological characteristics in terms of the miscibility, phase separation, crystallinity, and molecular packing for these four systems, a series of tests were performed. First, we dropped water and diiodomethane on the surface of the materials and measured their contact angles to explore the miscibility between the donors and acceptor (Fig. 4a), so as to calculate the surface tension (γ) of each material. After that, the Flory–Huggins interaction parameter χ^{D-A}, which could be used to quantify the miscibility between a donor and acceptor, was calculated *via* the equation of $\chi^{D-A} = (\sqrt{\gamma_D} - \sqrt{\gamma_A})^2$,[51,52] where a smaller χ^{D-A} value means better miscibility. As shown in Table 2, the χ^{D-A} values were 1.09 between D18 and BO-4T, 1.03 between PM6 and BO-4T, 0.66 between PBDB-T and BO-4T, and 0.83 between J52 and BO-4T, which means the miscibility of these four donors with BO-4T was in the order: PBDB-T > J52 > PM6 > D18. Over-mixing is not conducive to the formation of phase separation, leading to a greater risk of bimolecular recombination, while poor miscibility may tend to form over-large phase regions, leading to a greater risk of monomolecular recombination.

We then carried out atomic force microscopy (AFM) measurements to investigate the top surface morphological

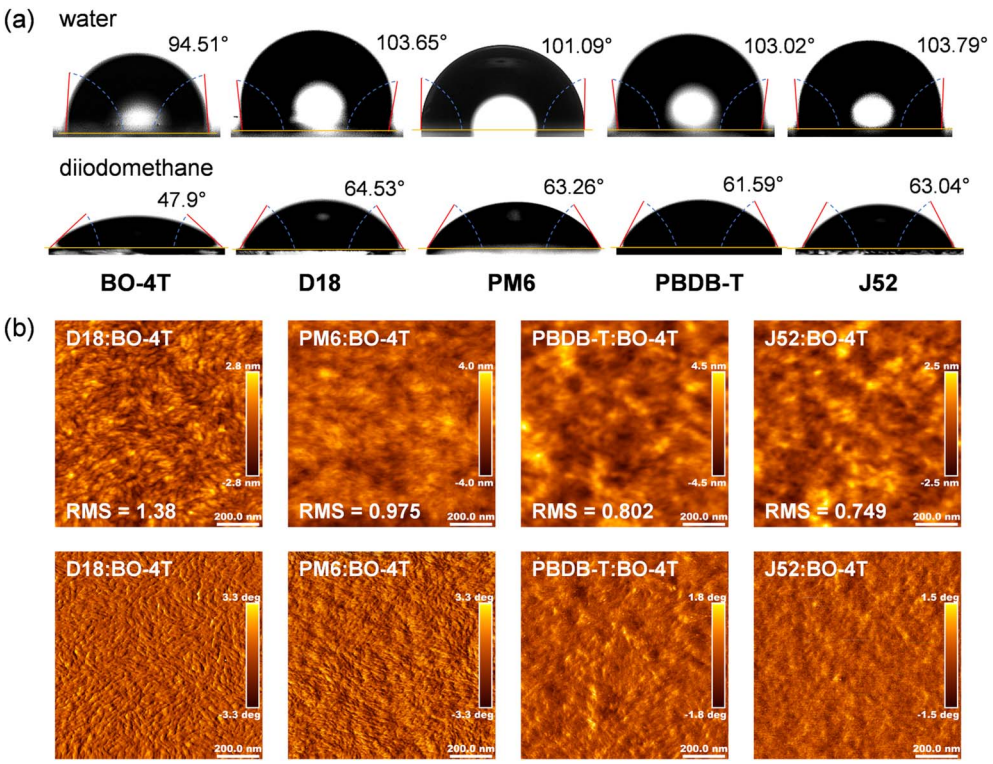

Fig. 4 (a) Contact angle images of BO-4T, D18, PM6, PBDB-T, J52 films with water and a diiodomethane droplet on top. (b) AFM height (top) and phase (bottom) images of D18:BO-4T, PM6:BO-4T, PBDB-T:BO-4T, J52:BO-4T films.

Table 2 Summary of the contact angles (θ), surface tensions (γ), and Flory–Huggins interaction parameters (χ) for BO-4T, D18, PM6, PBDB-T, and J52 films

Surface	θ_{water} (°)	θ_{DIM} (°)	γ (mN m^{-1})	χ^{D-A} [a]
BO-4T	94.51	47.9	57.34	—
D18	103.65	64.53	42.59	1.09
PM6	101.09	63.26	43.03	1.03
PBDB-T	103.02	61.59	45.70	0.66
J52	103.79	63.04	44.35	0.83

[a] The Flory–Huggins interaction parameter between the donor and acceptor was calculated through the equation of $\chi^{D-A} = (\sqrt{\gamma_D} - \sqrt{\gamma_A})^2$.

properties of the blend films (Fig. 4b). From the height images, we could find out that the root mean square (RMS) roughness values of the D18:BO-4T and PM6:BO-4T blend films were larger than that of the PBDB-T:BO-4T and J52:BO-4T blend films, which could be attributed to the fluorinated BDT unit enabling D18 and PM6 to have stronger crystallinity, thus resulting in stronger intermolecular aggregation. From the phase images, it could be identified that the PBDB-T:BO-4T and J52:BO-4T blend films showed well-mixed homogeneous surfaces due to the good miscibility between the donor and acceptor, which is conducive to the dissociation process, but with the risk of bimolecular recombination. This was, to some extent, the reason for the low FF of PBDB-T:BO-4T. This risk was also present for J52:BO-4T, but was compensated by the orientation and crystallization, as discussed later. While for D18:BO-4T and PM6:BO-4T films with reduced miscibility between the donor and acceptor, an obvious nanoscale phase-separation structure could be observed. However, relative to the PM6:BO-4T film, the phase separation in the D18:BO-4T film may be too large for mitigating monomolecular recombination and assisting exciton dissociation, thus resulting in the low J_{SC} and FF. Besides, PM6 had suitable miscibility with BO-4T to form suitable phase separation, which was conducive to exciton dissociation and the charge-transfer process, resulting in the best device performance.

Furthermore, GIWAXS characterization was performed to investigate the crystallinity and orientation of the blend films (Fig. 5 and Table S3†).[41] All the blend films exhibited dominant (010) diffraction peaks at $q_z = 1.84$ Å^{-1} ($d = 3.40$ Å) in the OOP direction, and the differences in π–π stacking distance among them were not significant. However, there were differences in the crystal coherence length (CCL). Among them, PM6:BO-4T and J52:BO-4T possessed relatively larger CCLs (29.2 Å and 29.1 Å, respectively), indicating the better crystallinity, which contributed to their higher FFs. While PBDB-T:BO-4T had the smallest CCL, which was not conducive to charge transport, corresponding to its lowest FF. In the IP direction, the (001) diffraction peaks could be observed at $q_r = 0.276$ Å^{-1} ($d = 22.8$ Å) for PM6:BO-4T and J52:BO-4T blends, and the PBDB-T:BO-4T blend was stacked a little closer with the (001) peak at $q_r = 0.330$ Å^{-1} ($d = 19.0$ Å). While the D18:BO-4T blend exhibited the largest lamellar spacing with the (001) peak at $q_r = 0.268$ Å^{-1} ($d = 23.4$ Å), which may give support to its lowest voltage loss as aforementioned.[53] It is noteworthy that the (002) peak, which originally appeared at $q_r = 0.452$ Å^{-1} ($d = 13.9$ Å) for the pristine acceptor, could also be found in the blend films, roughly as shown in the second dashed line in Fig. 5b, reflecting that the strong crystallization ability of the BO-4T allowed its stacking characteristics to be preserved to some extent in the blend film. In addition, the above films all exhibited a large proportion of face-on orientation characteristics, which was favorable for the charge transport and could, to some extent, be attributed to the face-on orientation of the BO-4T itself. The above results provide proof that the crystallization and orientation behavior

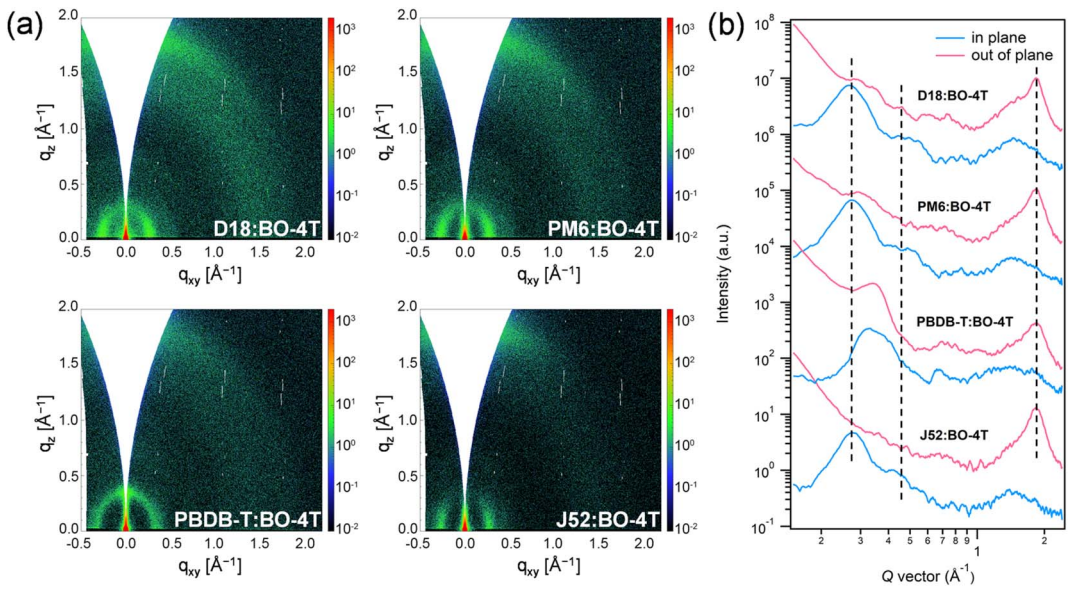

Fig. 5 (a) 2D GIWAXS images of the blend films. (b) GIWAXS intensity profiles of the corresponding films along the in-plane (blue lines) and out-of-plane (red lines) directions.

of the active layer can be effectively regulated by the rational structure design of the acceptors and carefully selected polymer donors.

Conclusions

We designed and synthesized a fully non-fused electron acceptor of BO-4T with a tetra-thiophene backbone and outward branched alkyl chains, based on which a systematic study was performed by mapping four polymer donors (D18, PM6, PBDB-T, J52) with BO-4T. The crystalline structure revealed that BO-4T possessed a planar skeleton and predominant face-on molecular orientation. As for D–A pairing principles, it was unveiled that, in an acceptable range, the narrowing energetic offsets were favorable for maximizing the voltage; with sufficient charge separation, the broadening absorption coverage in the short-wavelength range was beneficial for enlarging the photocurrent; besides, the relatively reduced miscibility between the donor and acceptor should be preferred for achieving phase separation for high crystallinity, but over-large domains must be avoided. Among the four polymer donors, PM6 worked the best with BO-4T, due to its greater benefits in voltage and FF. As a result, a high PCE of 14.33% was achieved for PM6:BO-4T-based OSCs, which is one of the highest efficiencies for OSCs based on NFREAs. This work may help researchers better understand the crystallization behaviors for NFREA-based blends, thus guiding the future design of highly efficient NFREAs.

Conflicts of interest

There are no conflicts to declare.

Acknowledgements

Q. Shen and C. He contributed equally. This work is supported by the National Natural Science Foundation of China (Nos. 52273199, 52127806, 21734008, 61721005, 52173185), the China Postdoctoral Science Foundation funded project (No. 2022M712737), research start-up fund from Zhejiang University and the Fundamental Research Funds for the Central Universities (No. 226-2022-00133, No. 226-2022-00209). The authors are grateful for the technical support for Nano-X from Suzhou Institute of Nano-Tech and Nano-Bionics, Chinese Academy of Sciences (No. C22006).

Notes and references

1 O. Inganas, *Adv. Mater.*, 2018, **30**, 1800388.
2 Y. Li, G. Xu, C. Cui and Y. Li, *Adv. Energy Mater.*, 2018, **8**, 1701791.
3 Y. Li, C. He, L. Zuo, F. Zhao, L. Zhan, X. Li, R. Xia, H. L. Yip, C. Z. Li, X. Liu and H. Chen, *Adv. Energy Mater.*, 2021, **11**, 2003408.
4 Y. Huang, E. J. Kramer, A. J. Heeger and G. C. Bazan, *Chem. Rev.*, 2014, **114**, 7006–7043.
5 C. He, Y. Pan, G. Lu, B. Wu, X. Xia, C. Q. Ma, Z. Chen, H. Zhu, X. Lu, W. Ma, L. Zuo and H. Chen, *Adv. Mater.*, 2022, **34**, 2203379.
6 M. Zhang, X. Guo, W. Ma, H. Ade and J. Hou, *Adv. Mater.*, 2015, **27**, 4655–4660.
7 Q. Liu, Y. Jiang, K. Jin, J. Qin, J. Xu, W. Li, J. Xiong, J. Liu, Z. Xiao, K. Sun, S. Yang, X. Zhang and L. Ding, *Sci. Bull.*, 2020, **65**, 272–275.
8 J. Yuan, Y. Zhang, L. Zhou, G. Zhang, H.-L. Yip, T.-K. Lau, X. Lu, C. Zhu, H. Peng, P. A. Johnson, M. Leclerc, Y. Cao, J. Ulanski, Y. Li and Y. Zou, *Joule*, 2019, **3**, 1140–1151.
9 C. Li, J. Zhou, J. Song, J. Xu, H. Zhang, X. Zhang, J. Guo, L. Zhu, D. Wei, G. Han, J. Min, Y. Zhang, Z. Xie, Y. Yi, H. Yan, F. Gao, F. Liu and Y. Sun, *Nat. Energy*, 2021, **6**, 605–613.
10 S. Li, L. Zhan, N. Yao, X. Xia, Z. Chen, W. Yang, C. He, L. Zuo, M. Shi, H. Zhu, X. Lu, F. Zhang and H. Chen, *Nat. Commun.*, 2021, **12**, 4627.
11 C. He, Z. Chen, T. Wang, Z. Shen, Y. Li, J. Zhou, J. Yu, H. Fang, Y. Li, S. Li, X. Lu, W. Ma, F. Gao, Z. Xie, V. Coropceanu, H. Zhu, J. L. Bredas, L. Zuo and H. Chen, *Nat. Commun.*, 2022, **13**, 2598.
12 L. Zhan, S. Li, Y. Li, R. Sun, J. Min, Y. Chen, J. Fang, C. Q. Ma, G. Zhou, H. Zhu, L. Zuo, H. Qiu, S. Yin and H. Chen, *Adv. Energy Mater.*, 2022, **12**, 2201076.
13 S. Li, L. Zhan, Y. Jin, G. Zhou, T. K. Lau, R. Qin, M. Shi, C. Z. Li, H. Zhu, X. Lu, F. Zhang and H. Chen, *Adv. Mater.*, 2020, **32**, 2001160.
14 C. He, Z. Bi, Z. Chen, J. Guo, X. Xia, X. Lu, J. Min, H. Zhu, W. Ma, L. Zuo and H. Chen, *Adv. Funct. Mater.*, 2022, **32**, 2112511.
15 Y. Cui, Y. Xu, H. Yao, P. Bi, L. Hong, J. Zhang, Y. Zu, T. Zhang, J. Qin, J. Ren, Z. Chen, C. He, X. Hao, Z. Wei and J. Hou, *Adv. Mater.*, 2021, **33**, 2102420.
16 L. Zuo, S. B. Jo, Y. Li, Y. Meng, R. J. Stoddard, Y. Liu, F. Lin, X. Shi, F. Liu, H. W. Hillhouse, D. S. Ginger, H. Chen and A. K. Jen, *Nat. Nanotechnol.*, 2022, **17**, 53–60.
17 C. He, Y. Pan, Y. Ouyang, Q. Shen, Y. Gao, K. Yan, J. Fang, Y. Chen, C.-Q. Ma, J. Min, C. Zhang, L. Zuo and H. Chen, *Energy Environ. Sci.*, 2022, **15**, 2537–2544.
18 Q. Shen, C. He, S. Li, L. Zuo, M. Shi and H. Chen, *Acc. Mater. Res.*, 2022, **3**, 644–657.
19 H. Fu, J. Yao, M. Zhang, L. Xue, Q. Zhou, S. Li, M. Lei, L. Meng, Z. G. Zhang and Y. Li, *Nat. Commun.*, 2022, **13**, 3687.
20 S. Li, C. Z. Li, M. Shi and H. Chen, *ACS Energy Lett.*, 2020, **5**, 1554.
21 Y. Liu, J. Song and Z. Bo, *Chem. Commun.*, 2021, **57**, 302–314.
22 J. Gao, X. Zhu, H. Bao, J. Feng, X. Gao, Z. Liu and Z. Ge, *Chin. Chem. Lett.*, 2022, 107968, DOI: **10.1016/j.cclet.2022.107968**.
23 M. Yang, W. Wei, X. Zhou, Z. Wang and C. Duan, *Energy Mater.*, 2021, **1**, 100008.
24 S. Li, L. Zhan, F. Liu, J. Ren, M. Shi, C. Z. Li, T. P. Russell and H. Chen, *Adv. Mater.*, 2018, **30**, 1705208.
25 Z. Zhang, S. Zhang, Z. Liu, Z. Zhang, Y. Li, C. Li and H. Chen, *Acta Phys.-Chim. Sin.*, 2019, **35**, 394–400.

26 Z. P. Yu, Z. X. Liu, F. X. Chen, R. Qin, T. K. Lau, J. L. Yin, X. Kong, X. Lu, M. Shi, C. Z. Li and H. Chen, *Nat. Commun.*, 2019, **10**, 2152.
27 Y. Zhou, M. Li, H. Lu, H. Jin, X. Wang, Y. Zhang, S. Shen, Z. Ma, J. Song and Z. Bo, *Adv. Funct. Mater.*, 2021, **31**, 2101742.
28 L. Ma, S. Zhang, J. Zhu, J. Wang, J. Ren, J. Zhang and J. Hou, *Nat. Commun.*, 2021, **12**, 5093.
29 Y. Liu, B. Liu, C.-Q. Ma, F. Huang, G. Feng, H. Chen, J. Hou, L. Yan, Q. Wei, Q. Luo, Q. Bao, W. Ma, W. Liu, W. Li, X. Wan, X. Hu, Y. Han, Y. Li, Y. Zhou, Y. Zou, Y. Chen, Y. Li, Y. Chen, Z. Tang, Z. Hu, Z.-G. Zhang and Z. Bo, *Sci. China: Chem.*, 2022, **65**, 224–268.
30 S. Li, L. Zhan, W. Zhao, S. Zhang, B. Ali, Z. Fu, T.-K. Lau, X. Lu, M. Shi, C.-Z. Li, J. Hou and H. Chen, *J. Mater. Chem. A*, 2018, **6**, 12132–12141.
31 S. Pang, X. Zhou, S. Zhang, H. Tang, S. Dhakal, X. Gu, C. Duan, F. Huang and Y. Cao, *ACS Appl. Mater. Interfaces*, 2020, **12**, 16531–16540.
32 C. Yang, L. Ma, Y. Xu, J. Ren, J. Hou and S. Zhang, *Sci. China: Chem.*, 2022, **65**, 2604–2612.
33 D. Luo, L. Li, Y. Shi, J. Zhang, K. Wang, X. Guo and A. K. K. Kyaw, *J. Mater. Chem. A*, 2021, **9**, 14948–14957.
34 W. Peng, G. Zhang, L. Shao, C. Ma, B. Zhang, W. Chi, Q. Peng and W. Zhu, *J. Mater. Chem. A*, 2018, **6**, 24267–24276.
35 Y. Geng, A. Tang, K. Tajima, Q. Zeng and E. Zhou, *J. Mater. Chem. A*, 2019, **7**, 64–96.
36 C. Zhang, X. Song, K. K. Liu, M. Zhang, J. Qu, C. Yang, G. Z. Yuan, A. Mahmood, F. Liu, F. He, D. Baran and J. L. Wang, *Small*, 2020, **16**, 1907681.
37 H. Zhao, H. B. Naveed, B. Lin, X. Zhou, J. Yuan, K. Zhou, H. Wu, R. Guo, M. A. Scheel, A. Chumakov, S. V. Roth, Z. Tang, P. Muller-Buschbaum and W. Ma, *Adv. Mater.*, 2020, **32**, 2002302.
38 H. Yao, Y. Cui, D. Qian, C. S. Ponseca Jr, A. Honarfar, Y. Xu, J. Xin, Z. Chen, L. Hong, B. Gao, R. Yu, Y. Zu, W. Ma, P. Chabera, T. Pullerits, A. Yartsev, F. Gao and J. Hou, *J. Am. Chem. Soc.*, 2019, **141**, 7743–7750.
39 D. Li, X. Zhang, D. Liu and T. Wang, *J. Mater. Chem. A*, 2020, **8**, 15607–15619.
40 C. He, Y. Li, S. Li, Z. P. Yu, Y. Li, X. Lu, M. Shi, C. Z. Li and H. Chen, *ACS Appl. Mater. Interfaces*, 2020, **12**, 16700–16706.
41 A. Mahmood and J. L. Wang, *Sol. RRL*, 2020, **4**, 2000337.
42 J. Mai, Y. Xiao, G. Zhou, J. Wang, J. Zhu, N. Zhao, X. Zhan and X. Lu, *Adv. Mater.*, 2018, **30**, 1802888.
43 C. He, Y. Li, Y. Liu, Y. Li, G. Zhou, S. Li, H. Zhu, X. Lu, F. Zhang, C.-Z. Li and H. Chen, *J. Mater. Chem. A*, 2020, **8**, 18154–18161.
44 G. Zhang, X. K. Chen, J. Xiao, P. C. Y. Chow, M. Ren, G. Kupgan, X. Jiao, C. C. S. Chan, X. Du, R. Xia, Z. Chen, J. Yuan, Y. Zhang, S. Zhang, Y. Liu, Y. Zou, H. Yan, K. S. Wong, V. Coropceanu, N. Li, C. J. Brabec, J. L. Bredas, H. L. Yip and Y. Cao, *Nat. Commun.*, 2020, **11**, 3943.
45 L. Ye, X. Jiao, M. Zhou, S. Zhang, H. Yao, W. Zhao, A. Xia, H. Ade and J. Hou, *Adv. Mater.*, 2015, **27**, 6046–6054.
46 H. Bin, Z.-G. Zhang, L. Gao, S. Chen, L. Zhong, L. Xue, C. Yang and Y. Li, *J. Am. Chem. Soc.*, 2016, **138**, 4657–4664.
47 F. D. Eisner, M. Azzouzi, Z. Fei, X. Hou, T. D. Anthopoulos, T. J. S. Dennis, M. Heeney and J. Nelson, *J. Am. Chem. Soc.*, 2019, **141**, 6362–6374.
48 R. Liao, X. Ma, C. Tang, Y. Liu, W. Zheng, Y. Ma, Q. Tu, W. Lin, Y. Yi and Q. Zheng, *J. Mater. Chem. A*, 2022, **10**, 23915–23926.
49 A. K. Kyaw, D. H. Wang, D. Wynands, J. Zhang, T. Q. Nguyen, G. C. Bazan and A. J. Heeger, *Nano Lett.*, 2013, **13**, 3796–3801.
50 I. Riedel, J. Parisi, V. Dyakonov, L. Lutsen, D. Vanderzande and J. C. Hummelen, *Adv. Funct. Mater.*, 2004, **14**, 38–44.
51 L. Ye, H. Hu, M. Ghasemi, T. Wang, B. A. Collins, J. H. Kim, K. Jiang, J. H. Carpenter, H. Li, Z. Li, T. McAfee, J. Zhao, X. Chen, J. L. Y. Lai, T. Ma, J. L. Bredas, H. Yan and H. Ade, *Nat. Mater.*, 2018, **17**, 253–260.
52 T. Zhang, H. Chen, C. Li, K. Lu, L. Zhang, A. Shokrieh, J. Zhang, G. Lu, S. Lei and Z. Wei, *J. Mater. Chem. A*, 2022, **10**, 8837–8845.
53 J. Wang, X. Jiang, H. Wu, G. Feng, H. Wu, J. Li, Y. Yi, X. Feng, Z. Ma, W. Li, K. Vandewal and Z. Tang, *Nat. Commun.*, 2021, **12**, 6679.